Science Advances

AAAS

advances.sciencemag.org/cgi/content/full/2/11/e1601473/DC1

Supplementary Materials for

Printed multifunctional flexible device with an integrated motion sensor for health care monitoring

Yuki Yamamoto, Shingo Harada, Daisuke Yamamoto, Wataru Honda, Takayuki Arie, Seiji Akita, Kuniharu Takei*

Published 23 November 2016, *Sci. Adv.* **2**, e1601473 (2016)
DOI: 10.1126/sciadv.1601473

This PDF file includes:

- fig. S1. Cross-sectional device schematic image.
- fig. S2. Electrical resistance change of Ag electrodes over the kirigami structure.
- fig. S3. Schematic image of reusable and disposable sensor sheets.
- fig. S4. Images of disposable and reusable sensor sheets.
- fig. S5. Electrical stability of EGaIn and Ag contact under motion.
- fig. S6. FEM simulation.
- fig. S7. Frequency dependence of three-axis acceleration sensor.
- fig. S8. Cycle test of electrical contacts between EGaIn and Ag electrodes.
- fig. S9. Thickness dependence of UV sensors.
- fig. S10. TFT characteristics under UV exposure.
- fig. S11. Circuit diagram of ECG recording.
- fig. S12. Measurement setup.
- fig. S13. Skin temperature measurements using the printed temperature sensor and an IR sensor.
- fig. S14. UV detection under simulated sunlight.

Supplementary Information

Device structure of the entire device

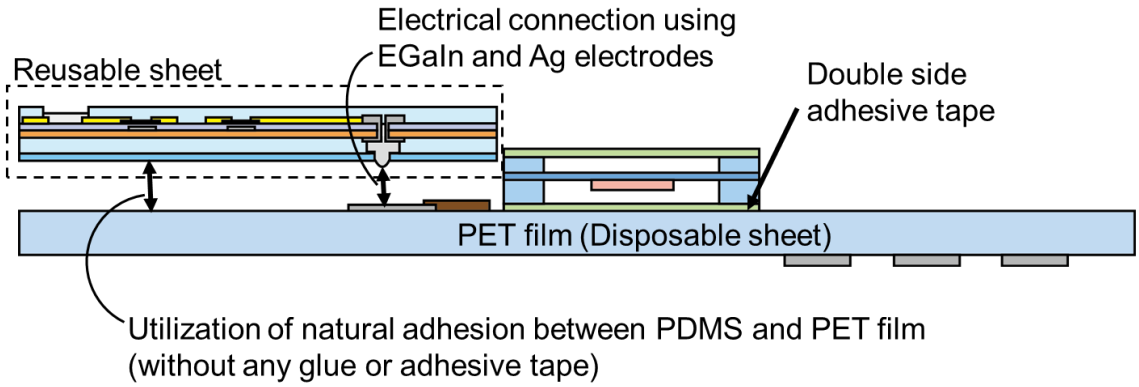

fig. S1. Cross-sectional device schematic image. Cross-sectional schematic of the device with explanation of adhesive materials to assemble each device component.

Electrical resistance change of Ag electrodes over the kirigami structure

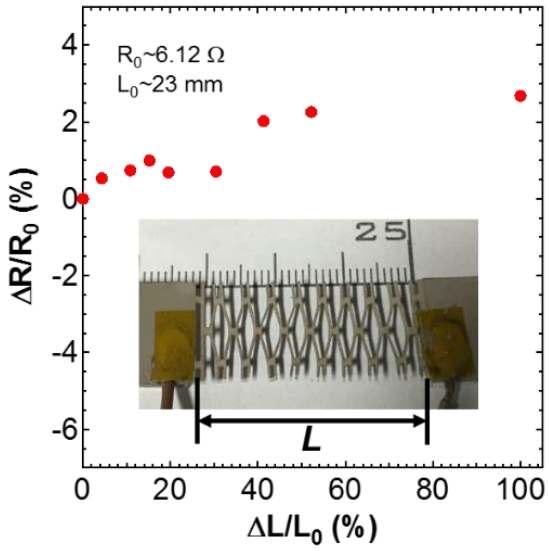

fig. S2. Electrical resistance change of Ag electrodes over the kirigami structure. Normalized resistance change ($\Delta R/R_0$) of printed Ag electrode over the kirigami structure as a function of stretchability ($\Delta L/L_0$), where ΔR is resistance change from original resistance of R_0 = ~6.12 Ω before stretching the substrate and ΔL is length change by stretching the kirigami structure shown in an inset photo from the original length of L_0 = ~23 mm.

Detail structure of electrical contacts between sheets

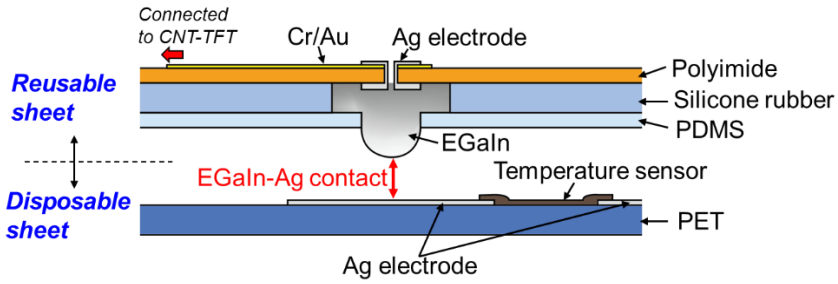

fig. S3. Schematic image of reusable and disposable sensor sheets. Schematic of reusable and disposable sensor sheets with detailed structure of EGaIn chamber and electrical contacts.

Disposable and reusable sheets

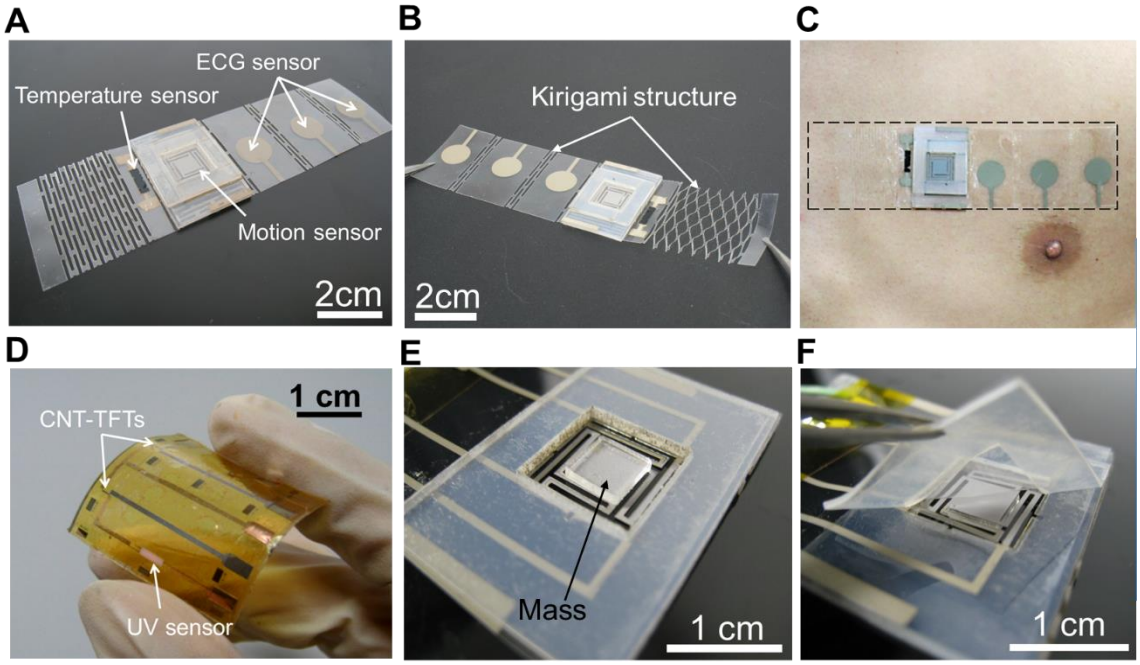

fig. S4. Images of disposable and reusable sensor sheets. (**A**) Disposable sheet integrated with temperature sensor, ECG sensor, and three-axis acceleration sensor. (**B**) Photograph of Kirigami structure, which allows significant stretching of the device. (**C**) Photograph of the disposable device sheet attached directly onto the skin. (**D**) Reusable sheet integrated with CNT-TFTs and UV sensor. Photographs of (**E**) backside and (**F**) topside of the acceleration sensor.

Electrical stability of EGaIn and Ag contact under motion

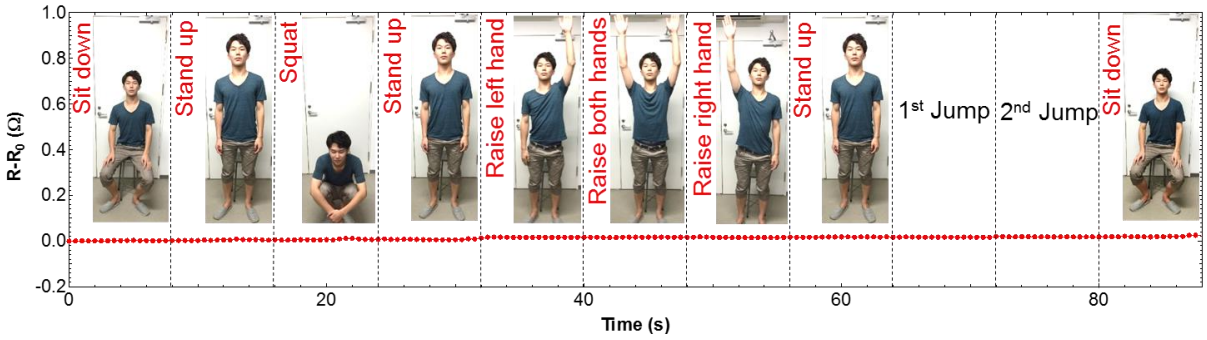

fig. S5. Electrical stability of EGaIn and Ag contact under motion. Resistance change of EGaIn and Ag contact under several motions. The device was attached on a chest. Photos inside the figure are just images of the actions for the measurements. R and R_0 are resistance during the actions and original resistance before actions.

Mechanical inflexibility of acceleration sensor region

In order to precisely measure acceleration induced by human motion, it is crucial that this sensor is mechanically inflexible: flexibility in the sensor region can alter the output signal as the strain values across the device differ when the structure is affected by different bending conditions — ultimately, this interferes with the signal generated by external movement. To address the challenge of integrating an inflexible component into an otherwise flexible device, we designed the structure of the acceleration sensor such that the flexible PET sheets sandwiched silicone rubber layers, as displayed in Fig. 2C: by taking the different values of Young's modulus for silicone rubber (760 kPa) and PET (2.45 GPa) into consideration, the design allows inflexibility in the acceleration sensing region, despite the fact that the device is mounted on mechanically flexible polymer materials (fig. S3).

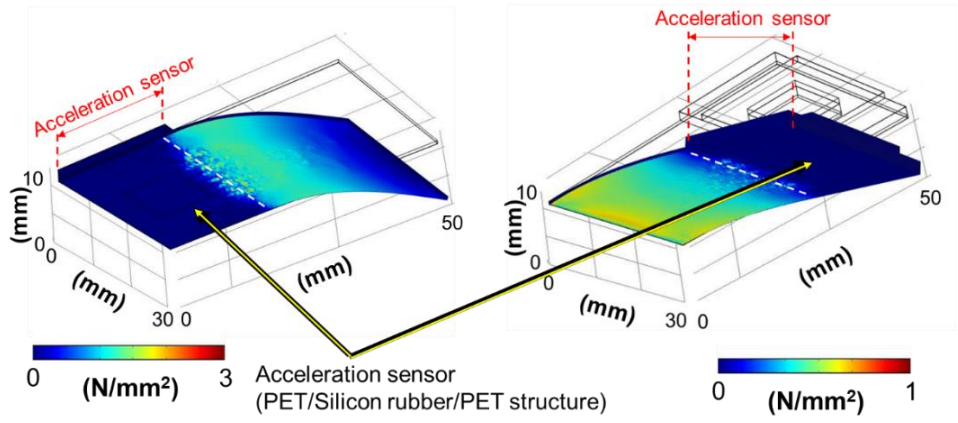

fig. S6. FEM simulation. The acceleration sensor possesses a PET/Silicon rubber/PET structure, which is mechanically inflexible (i.e. no stress under bending) due to strain engineering of the structure that exploits the different Young's moduli of the materials.

Resistance changes of the acceleration sensor

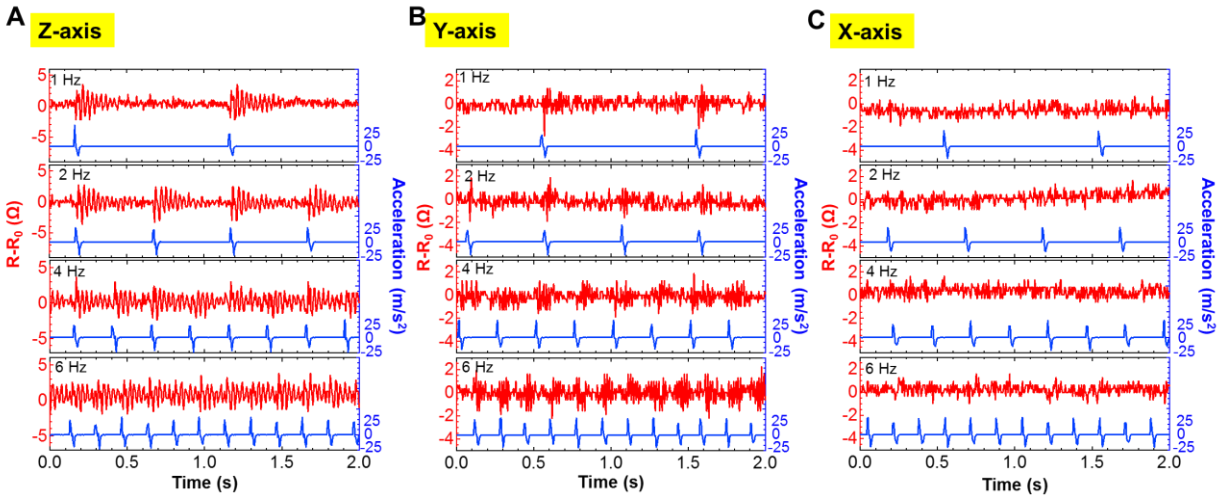

fig. S7. Frequency dependence of three-axis acceleration sensor. Resistance change at different acceleration frequencies measured from the strain Sensor #1 component of the acceleration sensor when acceleration is applied to (**A**) Z-, (**B**) Y-, and (**C**) X-axis.

Cycle test of electrical contacts of EGaIn between a reusable sheet and a disposable sheet

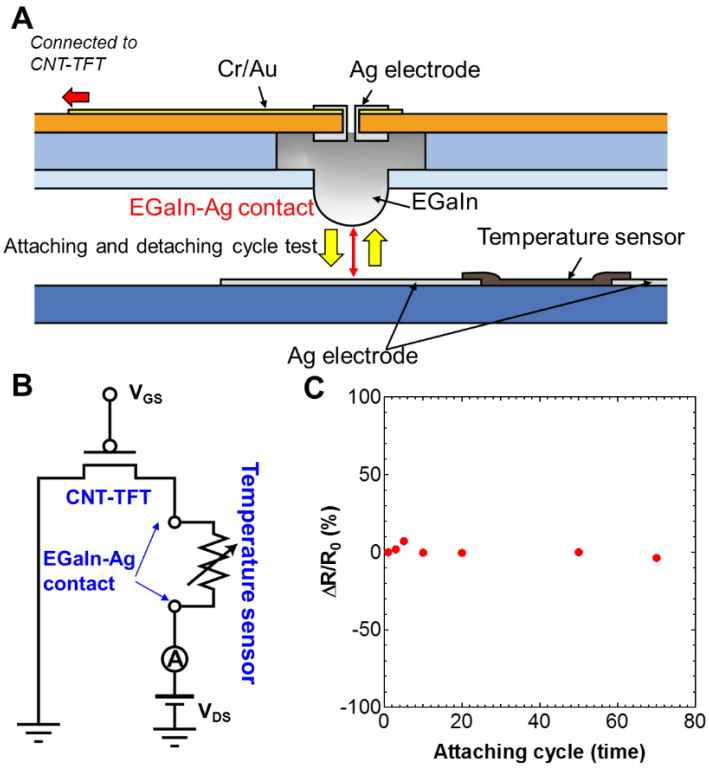

fig. S8. Cycle test of electrical contacts between EGaIn and Ag electrodes. (**A**) Schematic image of cycle test of electrical contact between EGaIn and Ag electrodes. (**B**) Measured electrical circuit diagram. (**C**) Resistance change ratio as a function of attaching cycles, where R_0 and ΔR are the initial resistance of the circuit as shown in (B) and the resistance change from R_0 after cycling test.

Response time of the UV sensor with different ZnO network film thickness

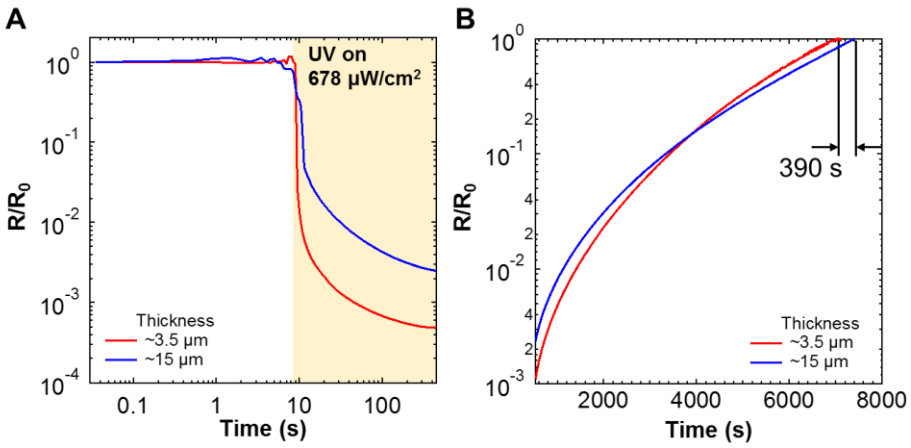

fig. S9. Thickness dependence of UV sensors. Response time of the UV sensors with different thickness of the ZnO network films when (**A**) UV light is exposed and (**B**) UV light is turned off.

On-resistance of CNT-TFT under UV exposure

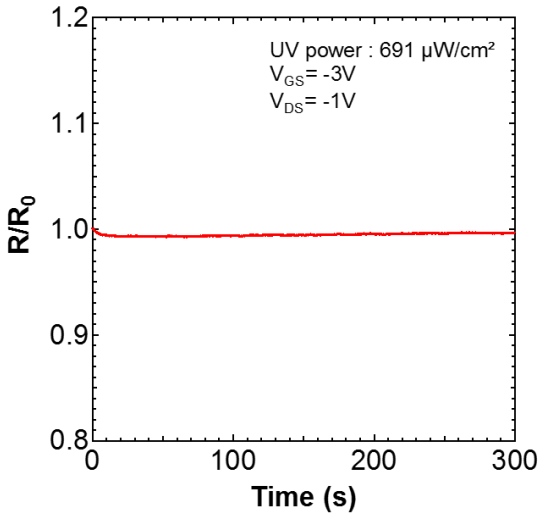

fig. S10. TFT characteristics under UV exposure. Real-time on-resistance change of CNT-TFT at $V_{GS} = -3$ V and $V_{DS} = -1$ V under UV light exposure. R_0 and R are on-resistance before UV exposure and after UV exposure, respectively.

Circuit diagram of ECG monitoring

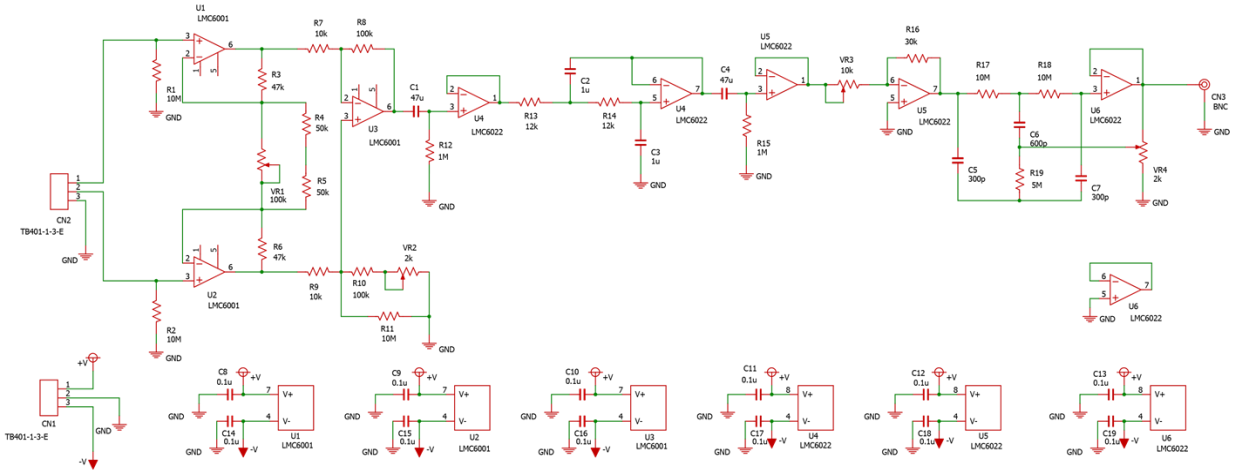

fig. S11. Circuit diagram of ECG recording. Circuit diagram of ECG monitoring used in this study. The filters are a high pass filter of 0.003 Hz, a low pass filter of 13.3 Hz, a high pass filter of 0.003 Hz, and a band rejection filter for 60 Hz.

Measurement setup

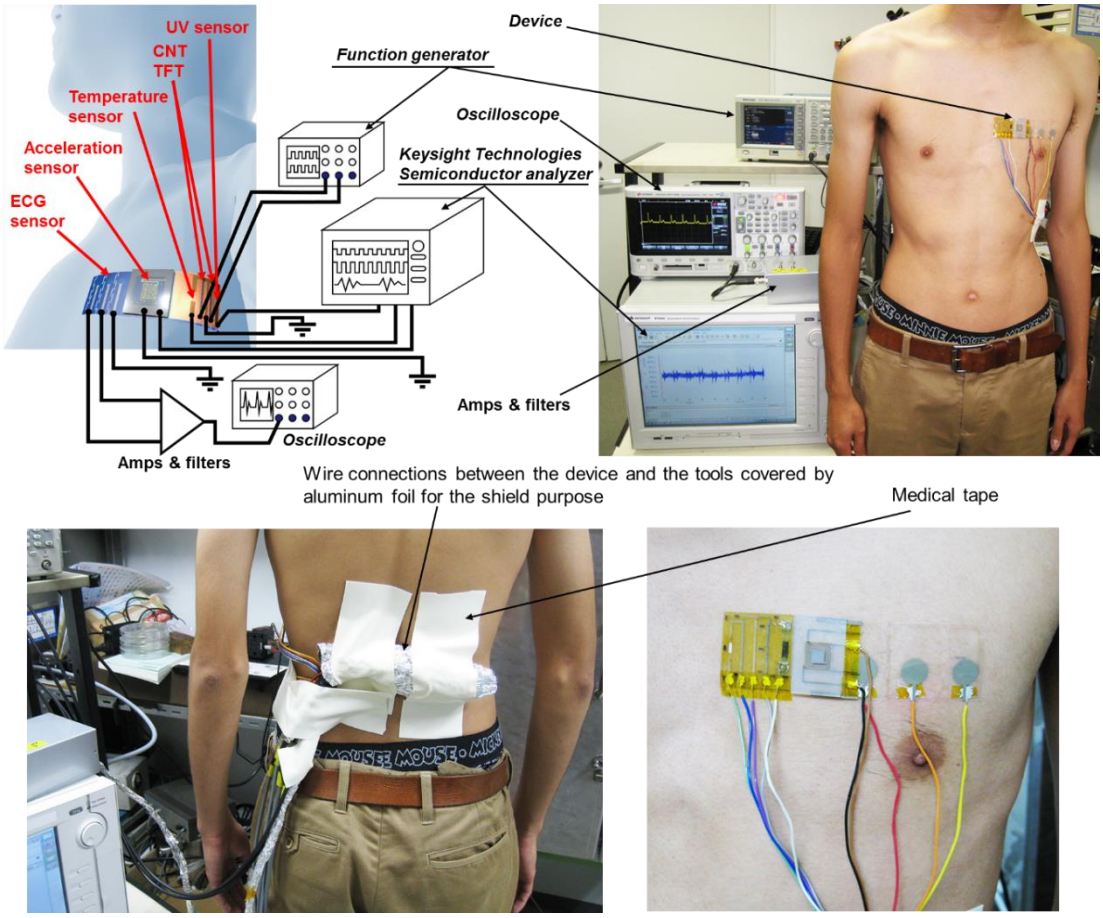

fig. S12. Measurement setup. Real-time health monitoring setup. ECG sensor was connected to an oscilloscope via amplifiers and filters to detect small signal of heartbeat. Outputs of the acceleration sensor, temperature sensor, and UV sensor were recorded by a semiconductor analyzer. For switching of CNT-TFTs, a function generator was used to apply gate bias for the both CNT-TFTs.

Skin temperature measured by the printed sensor and a commercially available IR sensor

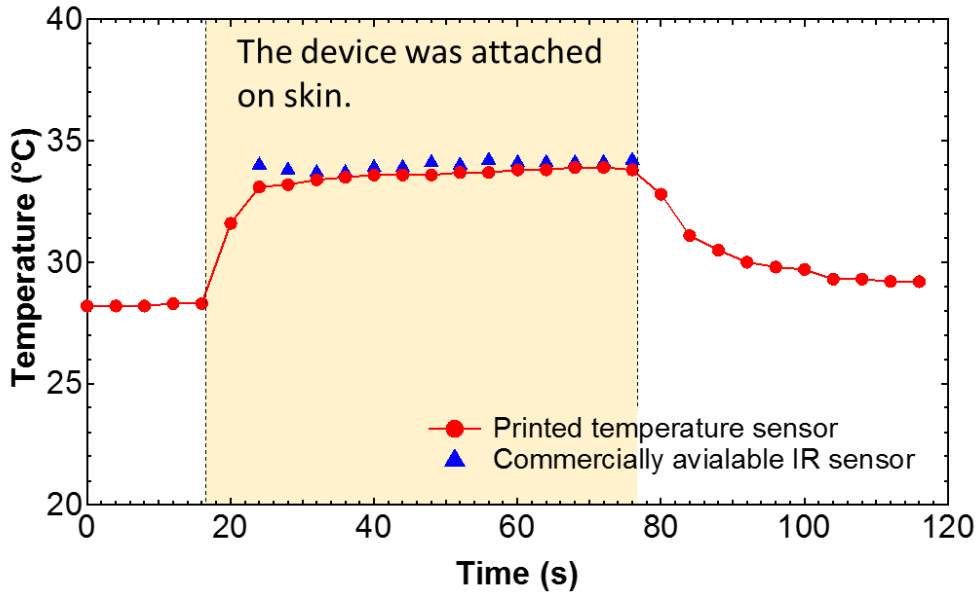

fig. S13. Skin temperature measurements using the printed temperature sensor and an IR sensor.

UV detection under sunlight generated by a solar simulator

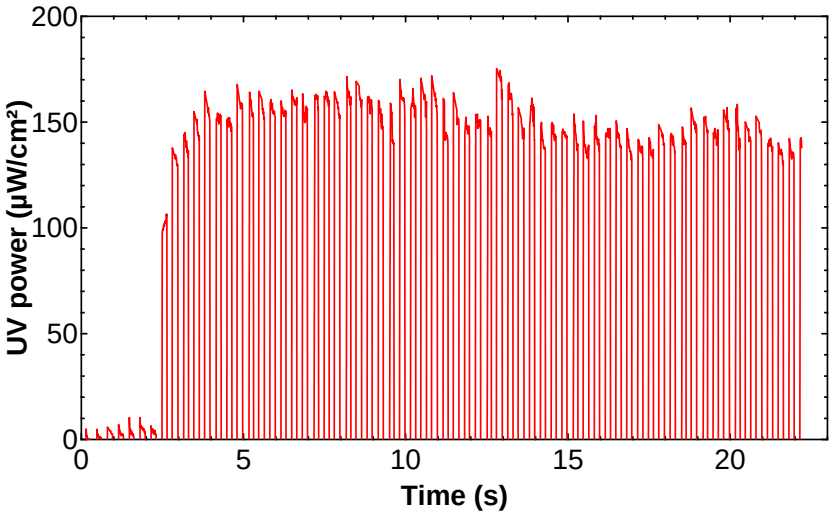

fig. S14. UV detection under simulated sunlight. UV power detection under ~50 mW/cm^2 sunlight generated by a solar simulator.